Journal Pre-proof

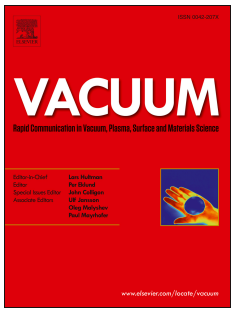

Characterization of sequential physical vapor deposited methylammonium lead tri-iodide perovskite thin films

J.N. Fru, N. Nombona, M. Diale

PII: S0042-207X(20)30588-1

DOI: https://doi.org/10.1016/j.vacuum.2020.109727

Reference: VAC 109727

To appear in: *Vacuum*

Received Date: 9 May 2020

Revised Date: 19 June 2020

Accepted Date: 19 August 2020

Please cite this article as: Fru JN, Nombona N, Diale M, Characterization of sequential physical vapor deposited methylammonium lead tri-iodide perovskite thin films, *Vacuum* (2020), doi: https://doi.org/10.1016/j.vacuum.2020.109727.

Characterization of Sequential Physical Vapor Deposited Methylammonium Lead Tri-Iodide Perovskite Thin Films

J. N. Fru[a], N. Nombona[b], M. Diale[a*]

[a]*Department of Physics, University of Pretoria, Private Bag X20, Hatfield 0028, South Africa*

[b]*Department of Chemistry, University of Pretoria, Private Bag X20, Hatfield 0028, South Africa*

Correspondence author's email and phone number: mmantsae.diale@up.ac.za, +27124204418

Abstract

Methylammonium lead tri-iodide perovskite ($MAPbI_3$) thin film for solar cells, **chemical formula $CH_3NH_3PbI_3$,** is synthesized in situ via sequential thermal vapor deposition of lead (II)iodide (PbI_2) and methylammonium iodide (MAI) single layers. The structural, morphological, optical, and electrical attributes are highly dependent on annealing time and MAI thickness. X-ray diffractograms confirmed the tetragonal crystal structure of $MAPbI_3$ with I4/mcm space group, good crystallinity which increases with the thickness of MAI and transformation of PbI_2-deficient $MAPbI_3$ to PbI_2-rich $MAPbI_3$ upon increasing annealing time. UV-Vis optical spectra reveal a redshift in the onset of absorption from 750 to 780 nm as the MAI thickness increases and a slight blueshift as the annealing time increases. Field emission scanning electron microscopy micrographs show densely packed polycrystalline grains with negligible pinholes and full coverage. The current density-voltage (*J-V*) characteristics under illumination reveals that the photogenerated current decreases with an increase in annealing time. Space charge limited current analysis of dark current *J-V* curves shows that PbI_2-deficient $MAPbI_3$ has higher mobility than PbI_2-rich $MAPbI_3$ and trap density increases with annealing time.

Keywords: Methylmmonium lead tri-iodide, sequential physical vapor deposition, thickness assessment, annealing time, perovskite solar cell.

1 Introduction

The fastest emerging third-generation solar cell technology is based on halide perovskites (HPs). They have desirable optoelectronic properties and versatile low-cost preparation options. Their outstanding

characteristics including extensive diffusion length [1], large carrier mobility [2], self-doping [3], low defect density [4], low phonon energy [5], ambipolar charge transport [6], broad absorption spectra [6], and tunable bandgap [7] are the driving forces behind the swift rise in performance of perovskite solar cells (PSCs). Just over a decade of intensive research, the power conversion efficiency (PCE) of PSCs has improved from 3.8 [8] to 24.2 % [9], which exceeds values for commercial multi-crystalline silicon (22.3 %) and copper indium gallium selenide (22.9 %) solar cells [10]. In addition to the upsurge in PCE, PSCs have flexible preparation methods that are fast and economical. These synthesis techniques comprise doctor blade [11], spin coating [12–14], physical vapour deposition [15], spray coating [16] , inkjet printing [17], meniscus printing [18], pulsed laser deposition [19], atomic layer deposition [20], meniscus-assisted solution printing [21] and dip coating [22]. Most solution-based methods are lab-scale, not suitable to implement in the fabrication of multi-junction tandem solar cells and produce low-quality films [23]. Physical vapour deposition (PVD), widely used in industry for thin film deposition is scalable, environmentally friendly and results in high-quality films [23]. Despite the surge in performance and low-cost processing methods, inherent instability, reproducibility, and scalability are major hindrances towards the commercialization of PSC technology. Factors affecting the stability of PSCs include moisture [24], high temperatures [25], UV-radiation [26], crystalline structure and stoichiometry [27]. These factors limit the lifetime of the devices to 3000 hours, which is very short compared to the lifespan of commercial silicon photovoltaics (25 years) [28]. The fundamental strategies being employed to improve the stability of perovskites solar cells include developing resilient halide perovskite and protecting the vulnerable absorbers with coatings [29]. Efforts to improve the stability of perovskites absorber are geared towards improving film quality [30] and developing stable stoichiometry [31]. Film quality can be improved by reducing grain boundaries (growing large grains), minimizing micro-strain density and producing densely packed grains to minimize leakage currents. Yang and co-workers [32] improved stability by passivating and minimizing grain boundaries. Zhao and co-workers [33] showed that the rate of degradation can be decreased by reducing residual strain. Likewise, Zhang and co-workers [30] showed that high quality films with large densely packed grains result in stable and high-performance PSCs.

Methylammonium lead tri-iodide ($MAPbI_3$), chemical formula $CH_3NH_3PbI_3$, is the best efficient and extensively investigated HP for solar cells. However, its preparation by PVD, which may improve its stability

and scalability, has rarely been exploited. Bonomi and co-workers [15] used RF-magnetron sputtering to prepare $MAPbI_3$ from single source containing methylammonium iodide (MAI)/lead(II)iodide (PbI_2). They achieved high purity films with full coverage within a large thickness range less than 200 nm to greater than 3 μm. Momblona and co-workers [34] synthesized $MAPbI_3$ films by co-evaporation PbI_2 and MAI from two separate crucibles. They obtained a homogenous morphology of smooth thin films resulting in PCEs of 15 %. The co-evaporation and single source approaches involve checking that rate of deposition. However, reproducibility is a problem since the deposition rates of powdered organic precursors are difficult to monitor because they are unsteady. The fluctuating rates are as a result of the small molecular weights of the precursors leading to random diffusion of the vapor molecules inside the enclosure [35]. Also, the rate of deposition may differ for various MAI precursors due to the presence of variable concentrations of methylammonium dihydrogen phosphide (MAH_2PO_3) and methylammonium hypophosphite (MAH_2PO_2) impurities [36]. On the contrary, the sequential physical vapor deposition (SPVD) approach is thickness regulated. Thickness monitoring using a quartz crystal monitor is more reproducible than the rate of deposition. One of the pioneering studies on SPVD involved the preparation of cesium lead tri-iodide ($CsPbI_3$) by alternate layer-by-layer deposition of CsI and PbI_2 [37]. This approach, though reproducible, is time-consuming as time is wasted during to alternate between several layers. There are a few reports on the growth of $MAPbI_3$ by SPVD. Miguel and co-workers [38] prepared $MAPbI_3$ using a system that automatically controls the source temperature and rate of deposition, and achieved phase pure films upon annealing at 140°C. The method still involves rate monitoring, which fluctuates for MAI and PbI_2 [35], hence difficult to reproduce. Patel and co-workers [39] slowed down the formation of $MAPbI_3$ during the SPVD of MAI on PbI_2 by lowering the substrate temperature to 0°C, which prevented inter-diffusion. By in-situ monitoring the absorption spectrum during the deposition process, they saw that nascent $MAPbI_3$ was formed as the substrate temperature was gradually increased due to the intermixing of MAI and PbI_2. However, ambient air was needed for the complete crystallization of $MAPbI_3$ and removal of excess MAI. Also, it is not clear what amounts (thicknesses) of MAI and PbI_2 where used in their experiment.

In this study, we prepared 3D $MAPbI_3$ thin films by SPVD of single layers of PbI_2 and MAI and optimized their structural, optical, morphological and electrical by varying the thickness of MAI and post-annealing

time. FTO/$MAPbI_3$/Au devices were fabricated and their *J-V* characteristics under dark measured. The characteristics were used to calculate the carrier mobility and trap density by the space charge limited current (SCLC) theory. This method is simplified, scalable, reproducible and paves the way for the preparation of stable thin $MAPbI_3$ films for solar cells.

2 Experimental details

Fig. 1 illustrates the set up for the preparation of $MAPbI_3$ thin films by SPVD of PbI_2 and MAI single layers using a resistive thermal evaporator. Microscopic glass substrates were trimmed into 15 x 20 mm and cleaned in acetone, isopropanol and deionized water respectively using an ultrasonic bath for 10 mins, to remove oils grease, and particle contaminations. Thereafter, they were dried by blowing with nitrogen gas remove moisture. PbI_2 (99.9 %) and MAI (0.42 M in 2-propanol) were obtained from Sigma Aldrich. The PbI_2 was used as received whereas the MAI solution was evaporated using a rotary evaporator to obtain a powder. Before deposition, the chamber was cleaned using a solution of extran diluted with deionized water (volume ratio 1:4) and high-pressure cleaner, to remove the effects of residual contaminants. The substrates were seated on to a holder and installed in the chamber. PbI_2 and MAI powder were inserted into separate cylindrical boron nitride boats, B_1 and B_2. The chamber was evacuated to a vacuum pressure of 2.0×10^{-5} mbar. The sequential deposition of the precursors was controlled by the switches, S1 and S2. The PbI_2 film was first deposited while switch S1 was closed and S2 opened, next MAI film was deposited while S2 and S1 are potentially interchanged, forming a layer of MAI on PbI_2. The thickness of PbI_2 was fixed at 100 nm while that of MAI was varied from 300 to 500 nm in steps of 100 nm. An inbuilt quartz crystal monitor, placed at the same level as the substrate inside the chamber, was used to monitor the thickness of thin film during the deposition process. The crystal monitor was calibrated for PbI_2 thickness measurement by setting the density to 6.16 g cm^{-3} and Z-factor to 1.10. Also, MAI film thickness was monitored by setting the density to 1.20 g cm^{-3} and Z-factor to 2.70. The crystallization of $MAPbI_3$ was accomplished by annealing the compound film at 100°C for 10 mins in an air-heated oven. The films grown using PbI_2 (99.9 %) and MAI (0.42 M in 2-propanol) are called SPL1**.** Finally, the experiment was repeated using PbI_2 (99.9 %) and MAI (98%) with MAI thickness maintained at 500 nm while annealing time was varied from 0 to 60 mins. The samples formed from PbI_2 (99.9 %) and MAI (98%) are called SPL2.

The XRD spectra of the thin films were measured by a Bruker D2-Phaser X-ray diffractometer using Cu Kα radiation with a wavelength of 0.15405 nm. The angle between the incident and diffracted rays, 2Θ, was varied from 10 to 50˚ in steps of 0.05. The measured spectra were used to determine the structure, crystallinity, crystallite size, micro-strain, and dislocation density of the films. The morphological properties were revealed by field emission scanning electron microscope (FE-SEM Zeiss Crossbeam 540), with an accelerating voltage of 2.0 kV. Grain size analyses were performed from the FE-SEM images following the American Standard for Testing Materials (ASTM) using the Image J software. The optical absorption spectra of the films were measured by CARY 100 BIO UV-Vis spectrometer with the wavelength of incident light in the 400-800 nm range. *J-V* measurements under illumination were performed using a Model 91150V Solar Simulator with solar output conditions of 100 mW cm^{-2} at 25℃ and Air-Mass 1.5 Global (AM 1.5 G) reference spectrum.

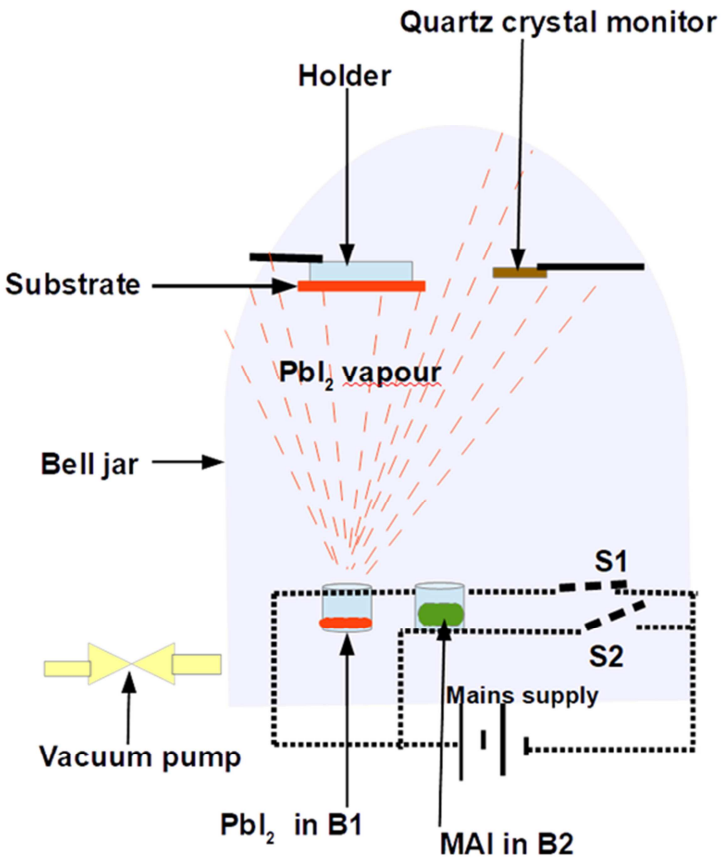

Fig. 1. Set up for the preparation of $MAPbI_3$ thin films by SPVD of PbI_2 and MAI single layers, adapted from Fru and co-workers [40].

3 Results and discussion

3.1 Structural properties

3.1.1 Structural properties of $MAPbI_3$ for various MAI thickness

Fig. 2 (a) displays the diffractograms of the synthesized SPL1 thin films for peculiar thicknesses of MAI. The patterns show fine peaks saying good crystallinity and the crystal structure was then indexed to the tetragonal crystal system of $MAPbI_3$, with I4/mcm space group [14,41–43]. Notably, Frohna and co-workers [44] demonstrated from first principle calculations that tetragonal $MAPbI_3$ is centrosymmetric at room temperature with I4/mcm space group. The intensity of the extra (001) diffraction peak is indexed to the PbI_2 residue according to JCPDS card number 07-0235. Additionally, it is seen to decrease with increase in the thickness of MAI. This shows that the phase-purity of $MAPbI_3$ increases as MAI thickness is increased. Fig. S1 (supporting information) has spectra for 50 nm PbI_2:350 nm MAI and 300 PbI_2:100 nm MAI. Particularly, the characteristic (110) and (220) peaks showing the formation $MAPbI_3$ were absent. However, when the thickness of PbI_2 is kept at 100 nm and that of MAI increased from 300 to 500 nm, the peaks for $MAPbI_3$ appeared. The intensities of (110) and (220) diffraction planes increase with MAI thickness as shown in Fig. 2 (a), indicating an increase in crystallinity of $MAPbI_3$. This is because increasing the thickness of MAI may increase the amount of carbon, hydrogen and iodine atoms that are needed at Wyckoff positions in the crystal lattice, bringing about high structure factor. The increase in peak intensity may also arise from a rise in the number of refection planes, which increases the multiplicity factor and hence the intensity. This is because each added layer of atoms contributes to the resultant intensity of the diffraction peaks because of coherent scattering. It is worth noting that the thickness ratio of PbI_2 to MAI that gave SPL1 is different from that obtained by Miguel and co-workers [38] using an automated SPVD method. The difference may come from the deposition parameters and conditions used.

The crystallite size and micro-strain were calculated from the Williamson-Hall (W-H) plot. The W-H plot is applied when the simultaneous contributions of crystallite size and micro-strain to X-ray line broadening is required [45]. The W-H relation is given by Equation 1,

$$\beta \cos\theta = \frac{K\lambda}{D} + 4\varepsilon \sin\theta \quad (1)$$

where D is the crystallite, β is the full width at half maximum, λ is the wavelength, θ is the Bragg's diffraction angle, ε is the micro-strain, K is the Scherrer constant which is determined by the crystallite shape and is considered as 0.94 for spherical crystallites with cubic symmetry. Fig. S2a shows the W-H plot for various MAI thicknesses. The micro-strains are obtained from the slopes while the crystallite sizes are calculated from the intercepts. The slopes are negative and decrease in magnitude as the thickness of MAI is increased, which indicates that the strains are compressive and decrease with MAI thickness as shown in Fig. 2 (c). Zhao and co-workers [33] showed that decrease in the micro-strain enhance hole extraction at the perovskites/hole transport layer interface by flattening the valence band. Furthermore, they pointed out that carrier mobility increases when micro-strains are removed. Jones and co-workers [46] showed that micro-strain promotes defect concentration in $MAPbI_3$ films and enhances non-radiative recombination. Therefore, the decrease in micro-strain is expected to reduce defect density and non-radiative recombination. The calculated average crystallite sizes increase with the thickness of MAI as shown in Fig. 2 (b), and the increase may be due to a decrease in micro-strain which is expected to cause a decrease in band gap.

The lattice constants are computed using Bragg's law (Equation 2) and the relationship between the interplanar spacing, d, and the Miller indices of a tetragonal crystal structure is given by Equation 3,

$$n\lambda = 2d \sin\theta \quad (2)$$

where $n = 1$.

$$\frac{1}{d^2} = \frac{h^2 + k^2}{a^2} + \frac{l^2}{c^2} \quad (3)$$

where *a* and *c* are the lattice constants and *(hkl)* are the miller indices. A least-square fitting procedure is used to extract the lattice constants of the $MAPbI_3$ for various MAI thicknesses and presented in Table 1. The results show that the unit cells increase continuously on the *c*-axis but contracts and then elongates as the thickness of MAI is increased from 300 to 500 nm. For the PbI_2-rich $MAPbI_3$ thin film having 100 nm PbI_2 and 300 nm MAI, the lattice constants are a = 8.881 and c = 12.479. Increasing the thickness of MAI from 300 to 400 nm causes the tetragonal structure to contract on the *a*-axis and elongates on the *c*-axis. As the thickness of MAI is increased beyond 400 nm, the unit cell elongates along both axes. The change in unit volume as thickness is increased correlates with changes in the micro-train which includes the peaks of PbI_2 shown in Fig. S3. The decrease in unit cell volume as the thickness of MAI is increased from 400 to 500 nm can be due to change of the micro-strain shown in Fig. S3 from tensile to compressive. The increase in volume as thickness is increased from 400 to 500 nm may be due to reduces in the size of the compressive micro-strain.

Table 1 Variation of lattice constants and unit cell volume of the SPL1 thin film with thickness of MAI.

Thickness of MAI (nm)	**Lattice constant, *a*, (Å)**	**Lattice constant, *b* (Å)**	**Lattice constant, *c* (Å)**	**Unit cell volume, *V* ($Å^3$)**
300	8.881	8.881	12.479	984.246
400	8.860	8.860	12.508	981.873
500	8.902	8.902	12.542	993.898

The dislocation density ρ, representing imperfections in the crystal, was calculated using the Williamson and Smallman formula given by Equation 4 [47],

$$\rho = \frac{n}{D^2} \quad (4)$$

where D is the crystallite size and n = 1 for minimum ρ. The dislocation density is seen to decrease continuously with increase in MAI thickness, when the peaks corresponding to PbI_2 are excluded in the calculation, as shown in Fig. 2 (d). Including the PbI_2 peaks reduces the ρ from 3.825 x 10^{11} cm^{-2} to 2.947 x 10^{11} cm^{-2} for the 300 nm MAI thick film. As the MAI film thickness is increased, there is a first increase in ρ and a later decrease. PbI_2-rich films have lower dislocation densities than PbI_2-deficient ($MAPbI_3$-pure) films as shown in Figure S3. Dislocations have been shown to reduce the performance of perovskites solar cells. Haque and co-workers [48] calculated the ρ of solution-processed caesium lead tri-iodide ($CsPbI_3$) solar cells and observed that cells with lowest ρ had the best PCE. Furthermore, the presence of defects generally lead to decrease in performance for HPs solar cells [49]. Therefore, the film having 500 nm thick MAI, with lowest ρ, may result in high performing solar cells.

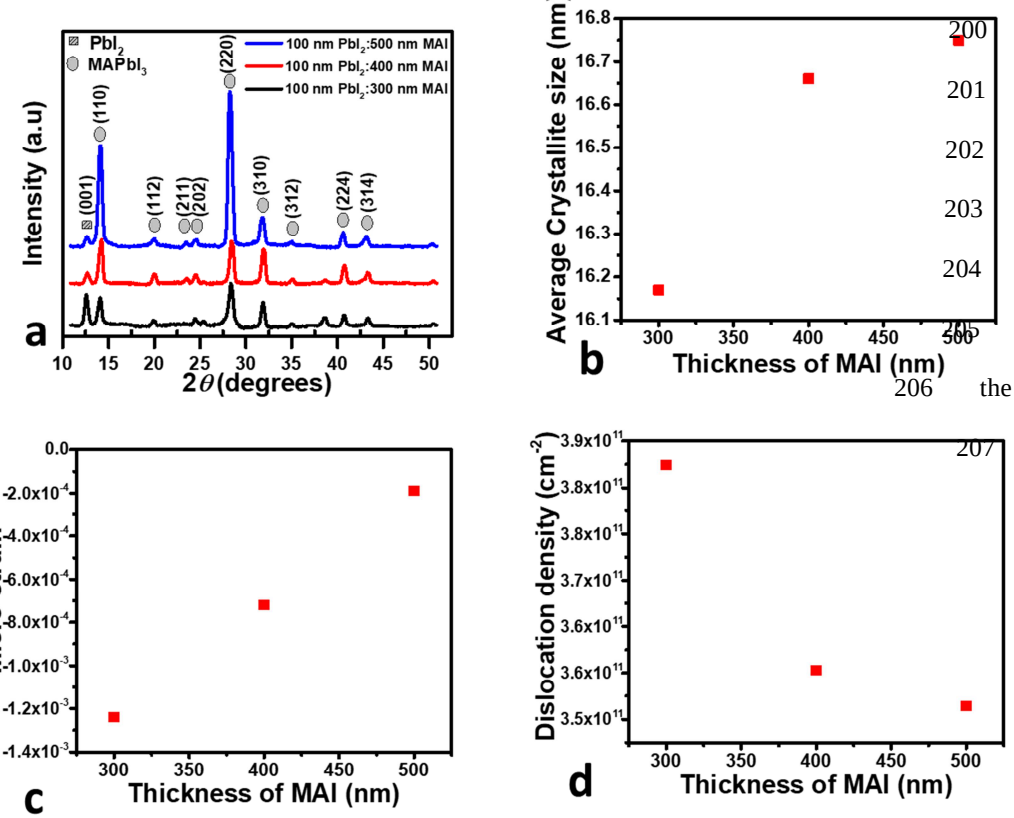

Fig. 2. (a) Diffractograms of the SPL1 thin films for peculiar thicknesses of MAI; (b) Micro-strain of the SPL1 thin film against MAI thickness; (c) Crystallite size of the SPL1 thin film against MAI thickness; (d) Dislocation density of SPL1 thin film against MAI thickness.

3.1.2 Structural properties of $MAPbI_3$ thin films for various annealing times

Fig. 3 shows the structural analysis of SPL2 thin films for various annealing times. The diffractograms show sharp peaks indicating good crystallinity and a strong dependence on annealing time as shown in Fig. 3 (a). In comparison, the crystal structures are tetragonal with I4/mcm space, like the results for SPL1 thin films, vide infra. The spectrum of the as deposited film reveals a pure tetragonal $MAPbI_3$ phase, showing that crystallization of the SPL2 thin film starts during the deposition. This could be possible because the temperature of the substrate (95℃) was within the range of annealing temperatures for $MAPbI_3$, thus MAI could diffuse into the voids in the PbI_6 octahedra framework and recrystallize to form $MAPbI_3$. The annealing temperature for the crystallization of $MAPbI_3$ is within a 90–105℃ range [50]. It is known that inter-diffusion of MAI and PbI_2 during vapor deposition is determined by the substrate temperature. Patel and co-workers [39] showed that inter-diffusion and reaction during vapor deposition can be prevented by lowering the temperature of the substrate to 0℃ before the deposition of MAI on the PbI_2 . They added that PbI_2 and MAI

240 are transformed to $MAPbI_3$ under vacuum at room temperature, but the reaction is incomplete as MAI residue
241 stays in the film. The MAI residue is completely converted to $MAPbI_3$ when the film is exposed to humid air
242 at 21℃, because moisture exposure makes the MAI more mobile. Also, they saw that longer annealing times
243 improved the crystallinity and absorbance continuously. During the first 20 mins of annealing our films, no
244 noticeable change in the phase purity is seen on the diffractograms. However, after 40 mins, a very intense
245 PbI_2 peak is seen, showing that annealing for a long time causes a transformation $MAPbI_3$ to PbI_2, consistent
246 with previous results [51]. As annealing continues from 40 to 60 mins, the intensity of the PbI_2 peak decreases
247 as the time, showing a possible retransformation of PbI_2 to $MAPbI_3$. The formation of PbI_2 during annealing
248 has also been seen by other authors. Chen and co-workers [51] showed that increasing the annealing time
249 beyond that needed to just complete the formation of $MAPbI_3$ leads to the release of PbI_2, which passivates
250 the grain boundaries, thus improving electrical properties and performance. Park and co-workers [52]
251 demonstrated that the formation of PbI_2 residues occurs during the annealing step of the reaction rather than at
252 the initial stages.

253 Fig. 3 (b) shows how the average crystallite size of SPL2 thin films vary with annealing time. The
254 crystallite size decreases slightly during the first 20 mins, then increase greatly after 40 mins before
255 decreasing to a value close to that seen after 20 mins. In comparison, the change in crystallite size follows the
256 same trend as the changing intensity of the PbI_2 peak. Thus, the fluctuations of the average crystallite size
257 with increase in annealing time may be due to the reversible phase transformations occurring in the sample.
258 Interestingly, we realized that the crystallite size is highest after 40 mins, when the PbI_2 peak is most intense.
259 Therefore, we think that the presence of PbI_2 residue in $MAPbI_3$ thin films increases the average crystallite
260 size.

261 Fig. 3 (c) shows how the micro-strain of SPL2 thin films vary with annealing time. The as deposited
262 films show a large negative (compressive) micro-strain that decreased (relaxes) slightly as time is increased
263 from 0 to 20 mins. Beyond 40 mins, the micro-strain changes again from tensile to compressive. The
264 dependence also shows a strong correlation with the changing intensity of the PbI_2 peaks. The tensile nature
265 of the micro-strain may have caused the large crystallite size in the presence of a large proportion of PbI_2
266 from the transformation of $MAPbI_3$.

Fig. 3 (d) shows that the dislocation density increases slightly during the first 20 mins of post-annealing, then decreases drastically between 20 and 40 mins before increasing again. The fluctuations in dislocation is also due to the continuous transformation between PbI_2 and $MAPbI_3$ phases as the annealing time is increased. In particular, the smallest dislocation density is seen after 40 mins of annealing when the (100) peak corresponding to PbI_2 is most intense. This points out that the dislocation density is lower for the PbI_2-rich $MAPbI_3$ films than for the PbI_2 deficient films. The presence of unreacted PbI_2 in $MAPbI_3$ thin film has previously been shown to have both positive and negative effects on the performance of solar cells. Jacobsson and co-workers [53] showed that PbI_2-deficient $MAPbI_3$ thin films have high crystalline quality and result in solar cells with high V_{oc}, however, their PCE is low due to MAI at grain boundaries which offer barriers to charge transport. Conversely, the solar cells having PbI_2-rich films showed the highest performance. Kwon and co-workers [54], on the other hand, demonstrated that pure $MAPbI_3$ (without PbI_2 residue) has high photon absorption and long carrier lifetimes which leads to more photogenerated current and high PCE.

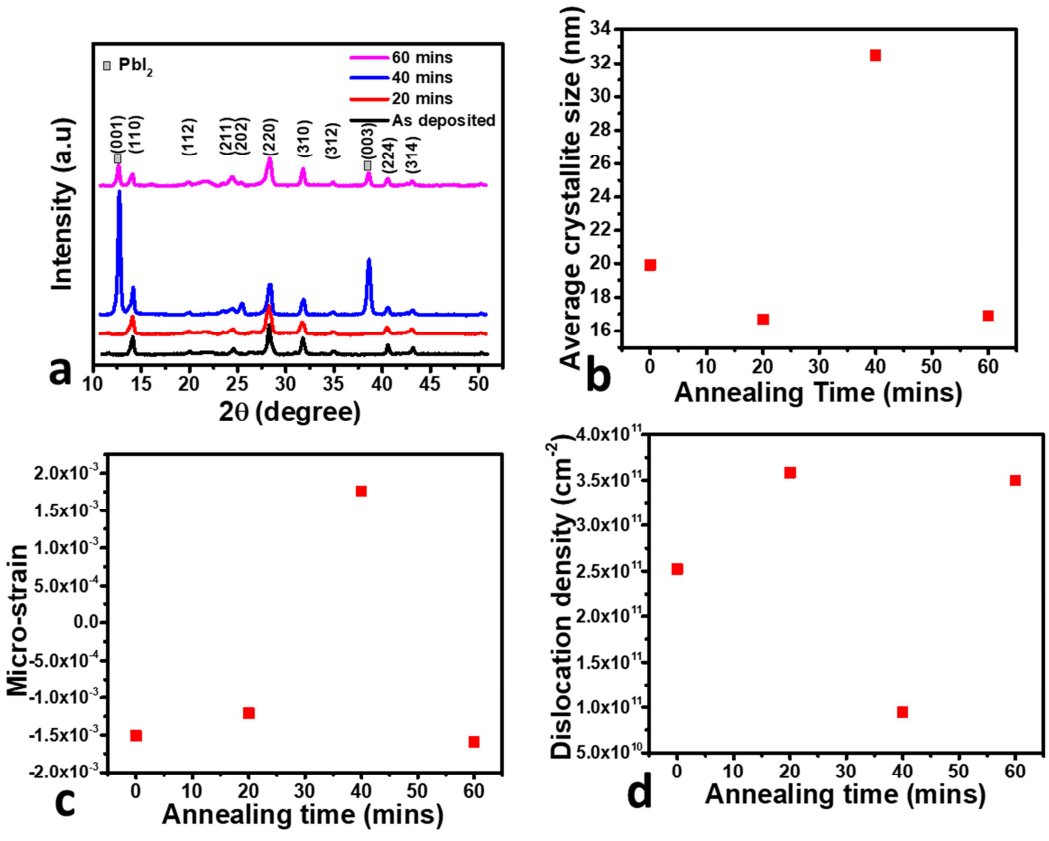

Fig. 3.

Structural analysis of SPL2 thin film having 400 nm thick MAI for various annealing times; (a) XRD diffractograms of SPL2 thin film against annealing times; (b) Average crystallite size of SPL2 thin films against annealing time; (c) Micro-strain of SPL2 thin film against annealing time; (d) Dislocation density of SPL2 thin films against annealing time.

Table 2 shows the lattice constants, unit cell volumes and grain sizes, depending on the annealing time, with non-linear relationships. The non-linear change in unit cell volume (*V*) with annealing time can be related to the effects of thermal expansion [55] and the phase transformations from $MAPbI_3$ to PbI_2, depicted by Fig. 3 (a), consistent with previous reports by Chen and co-workers [51]. As can be seen in Figure 3a and Table 2, the as deposited film is deficient of PbI_2 with lattice constants *a* and *c* equals 8.905 and 12.526 Å respectively. The lattice constants increase after 20 mins of annealing, leading to an increase in V of the unit cell, which may be due to thermal expansion during annealing. However, increasing the annealing time from 20 to 40 mins leads to a decrease in V and the sudden appearance of the very intense PbI_2 peak. This may be because the effect of phase transformation from $MAPbI_3$ to PbI_2 dominates that of thermal expansion and leads to a decrease in the decrease in V. Increasing the time to 60 mins reduces the intensity of the PbI_2 peak and there is a slight increase in V possibly due to thermal expansion.

Table 2 Variation of lattice constants, unit cell volume and grain size of SPL2 thin film for various annealing times.

Annealing time (mins)	**Lattice constant, *a* (Å)**	**Lattice constant, *b* (Å)**	**Lattice constant, *c* (Å)**	**Unit cell volume, V (Å^3)**	**Average grain size (nm)**
0	8.905	8.905	12.526	993.230	501.56± 36.47
20	8.924	8.924	12.553	999.693	413.07± 57.12
40	8.897	8.897	12.556	993.890	264.31±32.78
60	8.907	8.907	12.549	995.571	206.46±20.85

3.2 Morphological properties

3.2.1 Surface morphology analysis of $MAPbI_3$ for various MAI thicknesses

Fig. 4 presents the surface morphology of the synthesized SPL1 thin films for various MAI thicknesses. The films shown in Fig. 4 (a, b) were formed by deposition of 300 and 400 nm of MAI, respectively. Densely packed and randomly oriented grains were seen. The dense morphology is good for solar cells since photo-current leakage is presumably be minimized [56]. Furthermore, the grains have variable sizes and orientations. The variable orientations show that films are polycrystalline in nature. In addition, there was full coverage of substrate with negligible pinhole defects which may presumably reduce leakage current, increase open-circuit voltage and fill factor [57]. Likewise, the grain size increased from 150 to 180 nm corresponding to increased thickness from 300 to 400 nm of MAI. The grain size was not calculated for the sample with 500 nm MAI thickness films because the grains were not visible as observed in Fig. 4 (c). This could be a result of excess MAI, presumed covering the grains. The results showed that the average grain size is proportional to MAI thickness for all the samples. The increase in grain size will inevitably result in the fewer grain boundaries leading to reduced electron scattering and trap density [58]. Liu and co-workers [59] showed that reduction in trap density by passivating with polyhedral oligomeric silsesquioxane; which contains an amino group, improved device efficiency, open-circuit voltage and stability. We, therefore, deduce that the decrease in grain boundaries will lead to an increase in the stability.

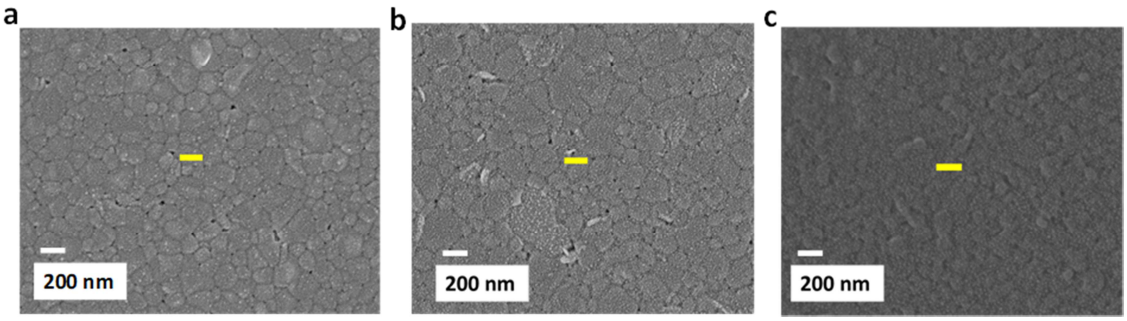

Fig. 4. The FE-SEM images of SPL1 thin film for various thickness of MAI; (a) Having 100 nm PbI_2 and 300 nm MAI thickness ratio; (b) Having 100 nm PbI_2 and 400 nm MAI thickness ratio; (c) Having 100 nm PbI_2 and 500 nm MAI thickness ratio.

3.2.2 Surface morphology analysis of $MAPbI_3$ for increasing annealing time

Fig. 5 is the SEM micrographs of SPL2 annealed in air at 100℃ for different times. All the films show densely packed randomly oriented pin-hole-free grains. Note that the difference in the average grain sizes of SPL2 (Fig. 5) and SPL1 (Fig. 4) may be based on the difference in purity of the MAI used in the deposition. The MAI powder precursor used for the preparation of the SPL1 is obtained by the evaporation of 2-propanol from 0.42 M solution of MAI while that for SPL2 is of 98 % purity and used as received. The average grain size decreases with an increase in annealing time as shown in Table 2. In particular, the average grain size for the as deposited is two times larger than that of film annealed after 40 mins. According to the XRD spectra, the as deposited film is PbI_2 deficient while the film annealed for 40 mins is rich in PbI_2. The decrease in average grain size maybe because of the transformation from $MAPbI_3$ to PbI_2. This agrees with Meerholz and co-workers [60] who showed that the effect of excess PbI_2 in precursor solution includes the accumulation of excess crystalline PbI_2 at grain boundaries and the surface, and the reduction in average grain size.

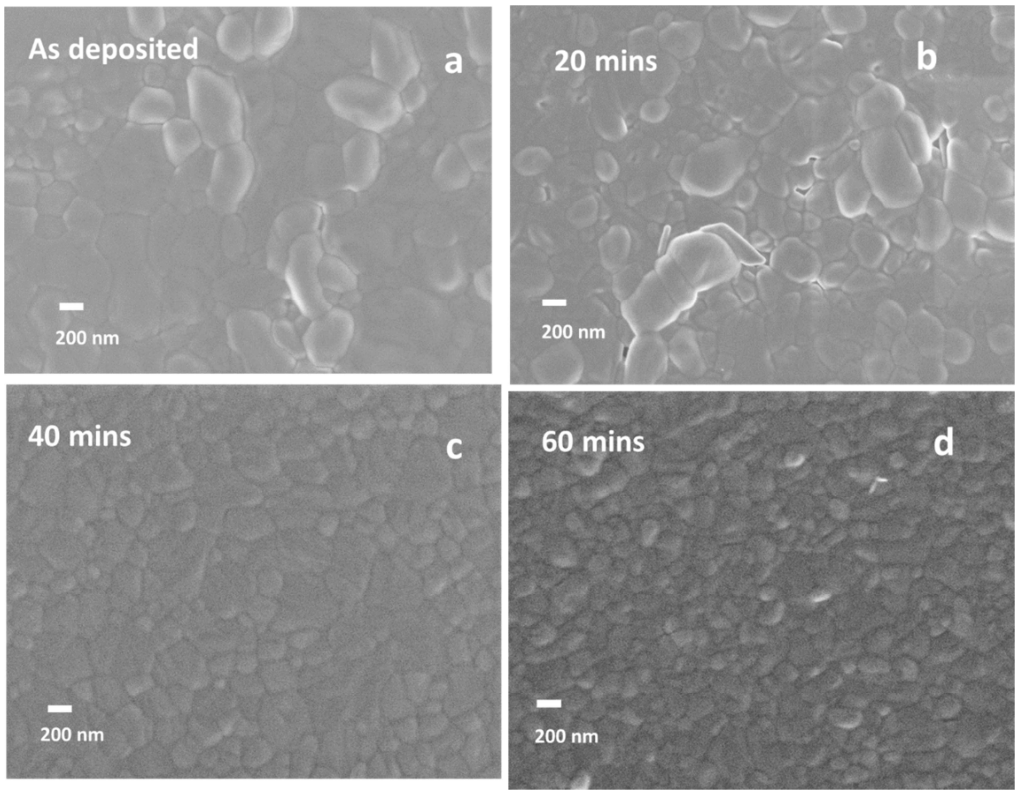

Fig. 5. FE-SEM micrographs of SPL2 thin films for various annealing times; (a) Micrograph of as deposited sample; (b) Micrograph of SPL2 thin film annealed for 20 mins; (c) Micrograph of SPL2 thin film annealed for 40 mins; (d) Micrograph of SPL2 thin film annealed for 60 mins.

3.3 Optical properties

3.3.1 UV-Vis absorption of $MAPbI_3$ for various MAI thickness

Fig. 6 (a) depicts the UV-Vis absorption spectra of SPL1 thin films for peculiar MAI thicknesses. Each spectrum shows a wide absorption band between 500 and 400 nm wavelengths, which agrees with the literature [61]. The absorption onset experiences a redshift as MAI thickness increases, which results in a decrease in direct and indirect bandgaps from 1.66 to 1.60 eV and 1.65 to 1.59 eV respectively, as shown in Fig. 6 (d). The decrease in bandgap may be due to the increase in crystallite size and tensile strain [62]. M. Oztas [62] observed that the energy bandgap of indium phosphide (InP) thin film is inversely related to the grain size and strain. Similarly, Innocenzo and co-workers [63] studied the relationship between morphology and luminescence properties of HPs and showed that optical bandgap decreased as crystallite size increased leading to longer carrier lifetimes. Furthermore, narrowing the bandgap is desirable to improve the PCE of the single-junction perovskite solar cells according to Shockley-Queisser theory [64]. Sha and co-workers [65] reported that the maximum PCE of 31 % is attained at the Shockley-Queiser optimum bandgap of 1.40 eV for single-junction PSCs. Therefore, better performing solar cells may be achieved when the bandgap approaches 1.40 eV. Likewise, bandgap reduction reduces the chances of creating deep level traps (recombination centers) in $MAPbI_3$ which may decrease carrier lifetimes [66].

The bandgap was computed using the Mott and Davis equation. Mott and Davis developed Tauc's idea of determining the bandgap of semiconductors. They proved that the optical absorption strength was proportional to the difference between photon energy and bandgap according to Equation 5 [67],

$$(\alpha h\upsilon)^{\frac{1}{n}} = A(h\upsilon - E_g) \quad (5)$$

where E_g is bandgap and A is a proportionality constant, α is the absorption coefficient, h is the Planck's constant, υ is the frequency, n is a numerical constant and its value determines nature of the transition; n

equals 1/2 , 2, 3/2, and 3 for direct allowed transitions, indirect allowed transitions, direct forbidden transitions and indirect forbidden transitions respectively. Fig. 6 (b, c) show the direct and indirect bandgaps from respective Tauc-plots, close to the absorption edge. In both cases, perfect fits are seen, indicating that the $MAPbI_3$ naturally exhibits both direct and indirect bandgap character, known as Rashba effect [68]. Etienne and co-workers [69] proved that the Rashba effect in HPs originates from splitting and shifting of the conduction band minimum in the *k*-space due to spin-orbit coupling. Rashba spin-orbit coupling has also been shown to enhance charge carrier lifetime in HPs [70].

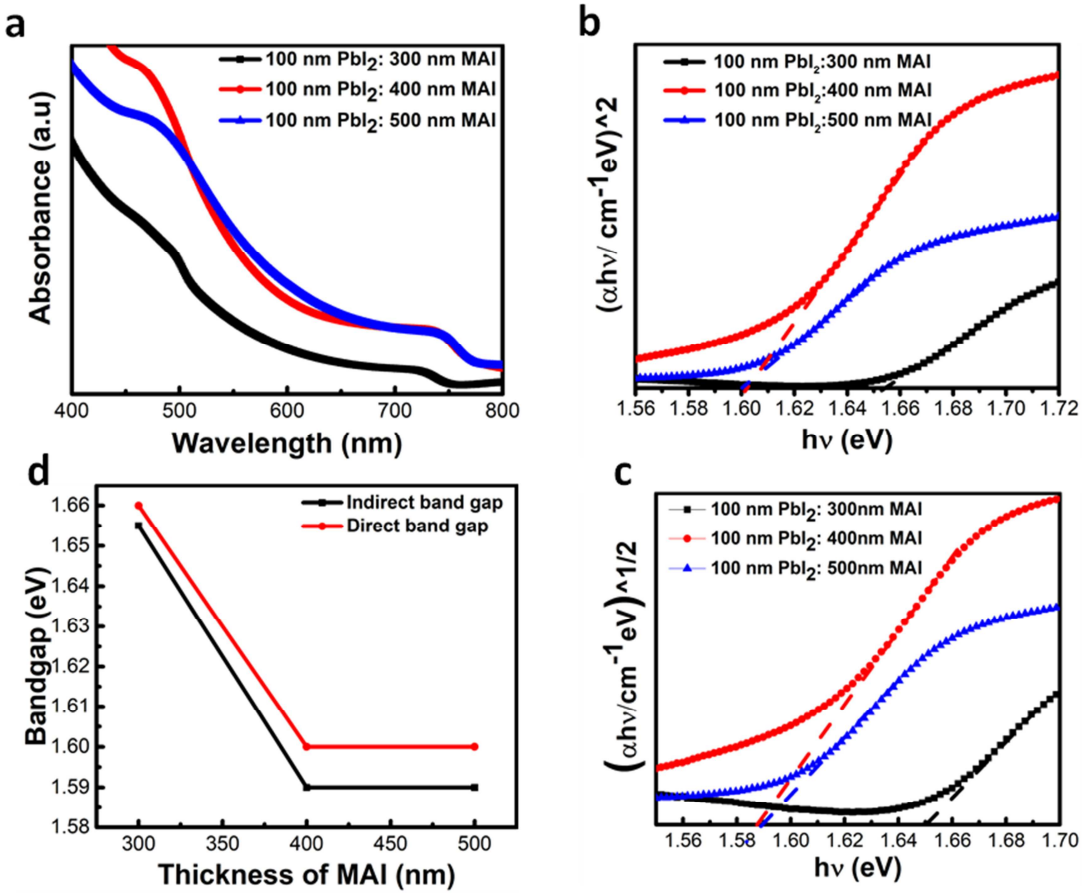

Fig. 6. (a) UV-Vis absorption spectra of SPL1 thin films for peculiar MAI thicknesses; (b) Direct bandgap Tauc-plot of SPL1 thin films for peculiar thicknesses; (c) Indirect bandgap Tauc-plot of SPL1 thin films for peculiar thicknesses; (d) Bandgap of SPL1 thin films against MAI thickness.

3.3.2 UV-Vis absorption of $MAPbI_3$ for varying annealing time

Fig. 7 (a, b) show the UV-Vis absorption spectra and direct bandgap Tauc-plot of the sequential physical vapour deposited thin SPL2 films respectively, for peculiar annealing times. The spectra of the films show an absorption edge close to 780 nm, which confirms the formation of $MAPbI_3$. However, the direct bandgap from Tauc-plot reveals a uniform increase with annealing time as shown in Fig. 7 (c). The increase in bandgap can be linked to the decrease in grain size as shown in Fig. 7 (d), consistent with the literature [71]. The increase in bandgap with annealing time may also be due to the presence of PbI_2, with absorption onset at 515 nm (large bandgap), [72,73], from the transformation of $MAPbI_3$ as the annealing time was increased. Increase in annealing time affects the absorbance differently in various regions of the visible spectrum. The absorbance of the as deposited thin film, which is deficient in PbI_2, is highest in the 500-800 nm range, while the absorbance of the film annealed after 40 mins is lowest in the same range. This indicates that the PbI_2-deficient $MAPbI_3$ then-films absorb more in the 500-800 nm range (visible range) than then PbI_2-rich thin-films, and this is consistent with previous reports by [54,73]. Kwon and co-workers proved that $MAPbI_3$ with excess PbI_2 has a lower absorbance than that of pure $MAPbI_3$ [54]. Similarly, Abdelmageed and co-workers showed that the intensity of visible light absorption decreased as more PbI_2 was produced from the degradation of MAPbI3 [73]. Fig. 7 (b) shows that the square of the product of absorption coefficient and energy decreases as annealing time increase. This implies that the absorption coefficient decreases with increase in annealing time and could be due to the presence of more PbI_2 in the thin SPL2 film, from the transformation of $MAPbI_3$ as the annealing time is increased.

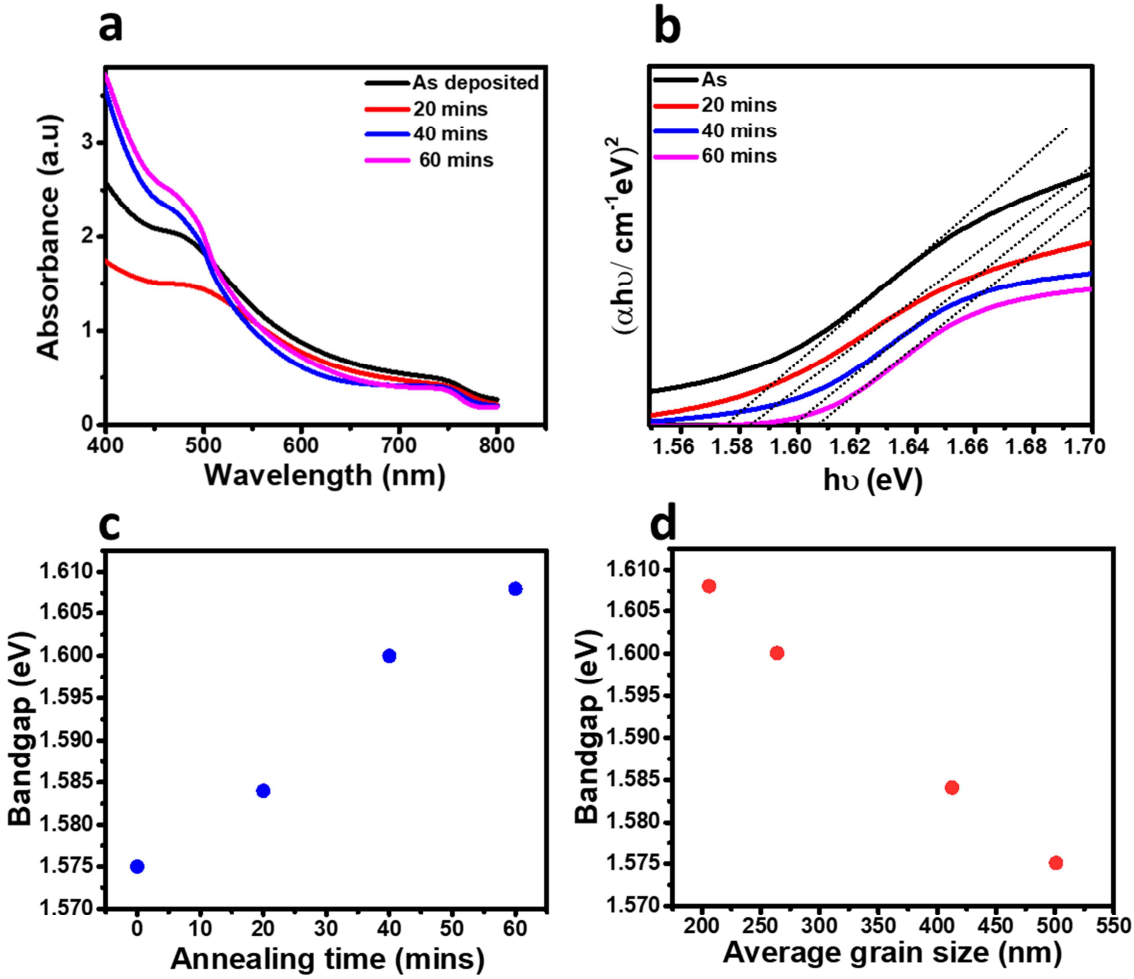

Fig. 7. (a) UV-Vis absorption spectra of thin SPL2 films for different annealing times; (b) Direct bandgap Tauc-plot of SPL2 for different annealing times; (c) Bandgap of thin SPL2 films vs. annealing time; (d) Bandgap of thin SPL2 films vs. average grain size.

3.4 Electrical properties

Fig. 8 shows the semi-logarithmic current density-voltage *(J-V)* characteristics under dark and light conditions for various FTO/SPL2/Au devices, where SPL2 the thin films are annealed at different times. The dark semi-log *J-V* plots are to verify the nature of the contacts and the possibility of using the space charge limited current (SCLC) theory to calculate the carrier mobility and trap density. All the curves are symmetric showing small barrier to charge carrier injection from the electrodes (ohmic contacts) and validating the

possible application of SCLC theory, in accordance with the literatures [13,74]. The quality of the ohmic contacts were determined by calculating the specific contact resistivity [75], ρ_c, which is the reciprocal of the gradient of the *J-V* curve as *V* turns to zero. The values of ρ_c are inversely related to the doping concentrations [76] and are displayed in Table 3. The small values of ρ_c reveal good ohmic contact [75], implying that SPL2 may be p-type materials, since p-type semiconductors make ohmic contacts with high work function metals like gold. The *J-V* measurements under illumination conditions were performed, with the devices exposed to solar simulated light of 1000 W m^{-2} intensity. The *J-V* measurements show that the current density for any given voltage under illumination conditions is higher in all the devices than the dark current density. This means that the SVP deposited $MAPbI_3$ HPs can generate charge carriers when exposed to sunlight, however, the amount of photogenerated charge carriers decreases with increase in PbI_2 produced during thermal annealing time. The as deposited SPL2 film generated the highest number of carriers when in forward bias. This is consistent with the UV-Vis spectrum of the sample which has the highest absorbance in the 500-800 nm visible range. The differences between the current densities under light and dark conditions are small. This narrow difference could be because the electric field at the p-n junction is weak such that the charge separation is ineffective.

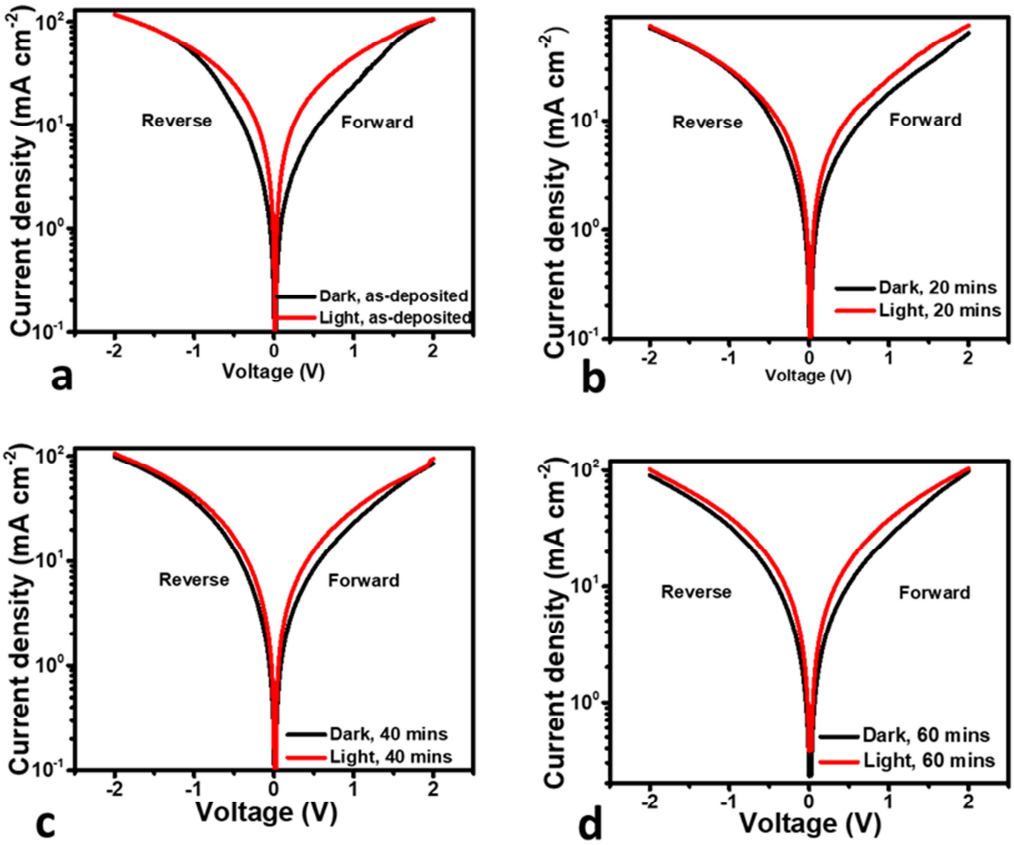

Fig. 8. Semi-log *J-V* characteristics of FTO/SPL2/Au devices under dark and illumination, where the SPL2 thin films are annealed at different times; (a) *J-V* curves of FTO/SPL2/Au devices having as deposited SPL2 thin film; (b) *J-V* curves of FTO/SPL2/Au devices having SPL2 thin film annealed for 20 mins; (c) *J-V* curves of FTO/SPL2/Au devices having SPL2 thin film annealed for 40 mins; (d) *J-V* curves of FTO/SPL2/Au devices having SPL2 thin film annealed for 60 mins.

The non-linear dark forward *J-V* characteristics suggest a power law dependence of *J* on *V* given by the Equation 6,

$$J \alpha V^{m} \quad (6)$$

where *m* is an exponent corresponding to the slope of the double-log *J-V* plot and reveals the bulk charge transport mechanism. Ohmic conduction is said to dominate when *m*~1, trap-free space charge limited current (SCLC) conduction dominates when *m* = 2 and trap limited SCLC conduction in the presence of traps exist when *m* > 2 [40]. During ohmic conduction, the current is driven by mobile charge carriers in the material. Thus, the carrier density needs to be known to calculate the mobility. Conversely, for SCLC conduction, the current is dominated by injected carriers from the contacts and it is solely dependent upon the mobility of the charge carriers that can be determined from a simple double-log *J-V* plot.

Fig. 9 is the double-log *J-V* characteristic of the FTO/SPL2/Au for different annealing times. The device containing as deposited SPL2 reveals ohmic transport and trap limited SCLC conduction as shown in Fig. 9 (a). The devices containing annealed SPL2 reveal ohmic transport and trap free SCLC conduction regions shown in Fig. 9 (b-d). As the biasing voltage is increased, charges are injected into the bulk of the $MAPbI_3$ leading to traps being filled continuously until the trap-filled limit (V_{TFL}) is reached, when all the traps are filled. The V_{TFL} is seen to increase with increase in annealing time as shown in Fig. 9. V_{TFL} is linked to the trap density N_t according to Equation 7,

$$V_{TFL} = qN_t \frac{d^2}{2\varepsilon_o\varepsilon_r} \quad (7)$$

where d is the film thickness, q is the electronic charge, ε_o is the permittivity of free space and ε_r is the dielectric constant of the $MAPbI_3$ is equal to 32 according to previous reports by Makhsud I Saidaminov and co-workers [77]. Since the V_{TFL} is directly proportional to N_t, it implies the N_t also increases with increase in annealing time. The calculated values for N_t increase as the annealing time increases and ranges from 3.25-4.55 x 10^{16} cm^{-3} as shown in Table 3. This can be because longer annealing times cause more trap charge carriers to gain enough energy to be released from localized states. The relationship between the current density and carrier mobility beyond the trap-filled limit is given by Equation 8,

$$J = \frac{9}{8}\varepsilon_o\varepsilon_r\theta\mu_p\frac{V^2}{d^3} \quad (8)$$

where J is the current density, V is the voltage at the onset of space charge limited region and θ is the trap factor, which is the ratio of free carriers to the sum of free and trapped carriers. θ is calculated by dividing the current at the onset of the space charge region by the current at the end [13,40,74] and results represented in Table 3. It increases with increase in annealing time and is consistent with the effect of annealing time on trap density. On the other hand, μ_p initially decreased after annealing for twenty mins, and then increased steadily with annealing time. This first decrease in μ_p may be because of the increase in N_t for the same $MAPbI_3$

phase. As heating continues beyond 20 mins, there is a transformation from $MAPbI_3$ to PbI_2 that may cause the mobility to increase slightly, even though the trap density increases. It can be deduced that PbI_2 deficient $MAPbI_3$ has a higher mobility than PbI_2-rich $MAPbI_3$.

Table 3 Variation of trap density, charge carrier mobility, trap factor and specific contact resistivity of SPL2 thin films with annealing time.

Annealing time (mins)	Trap density (cm^{-3})	Mobility ($cm^2 V^{-1} s^{-1}$)	Trap factor	Specific resistivity (Ωcm^2)
0	3.25×10^{16}	1.29	0.235	0.067
20	4.22×10^{16}	0.43	0.420	0.073
40	4.51×10^{16}	0.49	0.495	0.071
60	4.55×10^{16}	0.56	0.496	0.054

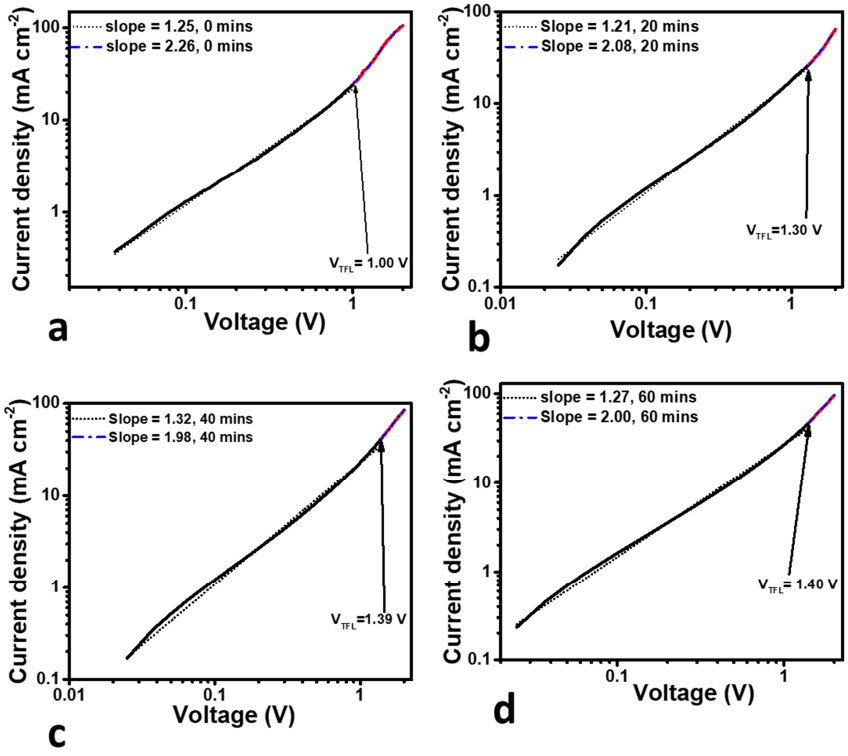

Fig. 9. Double-log *J-V* characteristics of FTO/SPL2/Au devices for which the SPL2 is annealed for different times; (a) Double-log *J-V* curves of FTO/SPL2/Au devices having as deposited SPL2; (b) Double-log *J-V* curve of FTO/SPL2/Au devices having SPL2 Annealed for 20 mins; (c) Double log J-V curves of FTO/SPL2Au devices having SPL2 annealed for 40 mins; (d) Double log *J-V* curves of FTO/SPL2/Au devices having SPL2 annealed for 60 mins.

4 Conclusions

We have demonstrated the preparation of thin $MAPbI_3$ films by SPVD of PbI_2 and MAI single layers. The structural, optical, morphological, and electrical properties were optimized by controlling the MAI film thickness and post-deposition annealing time. All the XRD diffractograms showed the tetragonal $MAPbI_3$ phase having the I4/mcm space group. The crystallinity was observed to increase with increase in MAI film thickness while prolonging the post-deposition annealing time resulted in the transformation of $MAPbI_3$ to PbI_2. Importantly, the unannealed films showed the pure $MAPbI_3$ phase, indicating crystallization started in situ during the deposition of MAI on PbI_2 at a substrate temperature of 95℃. The micro-strain and crystallite size increased, and dislocation density decreased with increase in MAI thickness while the changes of these properties with annealing time showed no regular pattern. FE-SEM results showed compact grains of variable sizes and orientations and with average grain size that increases with the thickness MAI but decreased with increased in post-annealing time. The reason for the decrease in average grain size with increasing post-annealing time, however, needs further investigation. Direct and indirect Tauc-plots of the UV-Vis absorption spectra showed a small Rashba effect, with optimum direct and indirect bandgaps of 1.60 and 1.59 eV, respectively. Also, the bandgap increased, and absorption intensity decreased with increase in annealing time. We observed that films containing PbI_2 produced during post-annealing showed lower absorption intensity. The trap density was observed to decrease with increase in annealing time and the maximum charge carrier mobility of 1.29 $cm^2\ V^{-1}\ s^{-1}$ was obtained for the unannealed film. The *J-V* characteristics under illumination

also revealed that the unannealed film had the highest photogenerated current. Based on our findings, we recommend the optimal thickness of 100 nm PbI_2 and 500 nm MAI and no post-annealing for low trap density, high charge carrier mobility, and pure thin $MAPbI_3$ films by SVPD.

Supporting Information

Three supporting figures: XRD spectra showing films with a ratio of PbI_2 to MAI greater than one and films with a ratio of PbI_2 to MAI less than one, W-H plots of $MAPbI_3$ for various thicknesses of MAI and various annealing times. average crystallite size, micro-strain, the dislocation density of $MAPbI_3$ for various MAI thickness with the effect extra PbI_2 peaks included.

Acknowledgements

The authors wish to thank the University of Pretoria, National Research Foundation-The World Academy of Science (NRF-TWAS) and NRF grant no N01156/115463 of the SARChI for financial support.

References

[1] Q. Dong, Y. Fang, Y. Shao, J. Qiu, L. Cao, J. Huang, Electron-hole diffusion lengths >175 μm in solution-grown $CH_3NH_3PbI_3$ single crystals, Sci. 347 (2015) 967-970. doi.10.1126/science.aaa5760.

[2] C. Wehrenfennig, G.E. Eperon, M.B. Johnston, H.J. Snaith, L.M. Herz, High charge carrier mobilities and lifetimes in organolead trihalide perovskites, (2014) 1584–1589. doi:10.1002/adma.201305172.

[3] Q. Wang, Y. Shao, H. Xie, L. Lyu, X. Liu, Y. Gao, J. Huang, Qualifying composition dependent p and n self-doping in $CH_3NH_3PbI_3$, Appl. Phys. Lett. 105 (2014) 163508. doi:10.1063/1.4899051.

[4] H. Tsai, R. Asadpour, J. Blancon, C.C. Stoumpos, O. Durand, J.W. Strzalka, B. Chen, R. Verduzco, P.M. Ajayan, S. Tretiak, J. Even, M.A. Alam, M.G. Kanatzidis, W. Nie, A.D. Mohite, Light-induced lattice expansion leads to high-efficiency perovskite solar cells, Sci. 360 (2018) 67-70. doi.10.1126/science.aap8671.

[5] T. Kirchartz, T. Markvart, U. Rau, D.A. Egger, Impact of small phonon energies on the charge-carrier lifetimes in metal-halide perovskites, J. Phys. Chem. Lett. 9 (2018) 939-946. doi.org/10.1021/acs.jpclett.7b03414.

[6] Z. Yu, L. Sun, Recent progress on hole-transporting materials for emerging organometal halide perovskite solar cells, Adv. Energy Mater. 5 (2015) 1500213. doi.org/10.1002/aenm.201500213.

[7] L. Wang, G.D. Yuan, R.F. Duan, F. Huang, T.B. Wei, Z.Q. Liu, J.X. Wang, J.M. Li, Tunable bandgap in hybrid perovskite $CH_3NH_3Pb(Br_{3-y}X_y)$ single crystals and photodetector applications, AIP Adv. 6 (2016) 045115. doi.org/10.1063/1.4948312.

564 [8] A. Kojima, K. Teshima, Y. Shirai, T. Miyasaka, Organometal halide perovskites as visible-light
565 sensitizers for photovoltaic cells, J. Am. Chem. Soc. 131 (2009) 6050. doi.org/10.1021/ja809598r.

566 [9] M.A. Green, M. Yoshita, E.D. Dunlop, D.H. Levi, J. Hohl-Ebinger, M. Ho-Yoshita, A.W.Y. Baillie,
567 Solar cell efficiency tables (version 54), Prog. Photovolt. Res. Appl. 27 (2019) 565-575.
568 doi.org/10.1002/pip.2978.

569 [10] M.A. Green, Y. Hishikawa, E.D. Dunlop, D.H. Levi, J. Hohl-Ebinger, M. Yoshita, A.W.Y. Ho-
570 Baillie, Solar cell efficiency tables (version 51), Prog. Photovolt. Res. Appl. 26 (2019) 3-12.
571 doi.org/10.1002/pip.2978.

572 [11] Y. Deng, E. Peng, Y. Shao, Z. Xiao, Q. Dong, J. Huang, Scalable fabrication of efficient organolead
573 trihalide perovskite solar cells with doctor-bladed active layers, Energy Environ. Sci. 8 (2015) 1544-
574 1550. doi 10.1039/c4ee03907f.

575 [12] P. Docampo, J.M. Ball, M. Darwich, G.E. Eperon, H.J. Snaith, Efficient organometal trihalide
576 perovskite planar-heterojunction solar cells on flexible polymer substrates, Nat. Commun. 4 (2013) 1-
577 6. doi.org/10.1038/ncomms3761.

578 [13] Y. Liu, F. Li, Z. Chen, T. Guo, C. Wu, T. Whan, Resistive switching memory based on
579 organic/inorganic hybrid perovskite materials, Vaccum. 130 (2016) 109–112.
580 doi:10.1016/j.vacuum.2016.05.010.

581 [14] S. Feng, D. Ding, A. Runa, T. Liu, P. Su, W. Yang, Enhanced photovoltaic property and stability of
582 perovskite solar cells using the interfacial modified layer of anatase TiO_2 nanocuboids, Vacuum. 166
583 (2019) 255–263. doi:10.1016/j.vacuum.2019.05.025.

584 [15] S. Bonomi, D. Marongiu, N. Sestu, M. Saba, M. Patrini, G. Bongiovanni, L. Malavasi, Novel physical
585 vapor deposition approach to hybrid perovskites: Growth of $MAPbI_3$ thin films by RF-magnetron
586 sputtering, Sci. Rep. 8 (2018) 1-8. doi.org/10.1038/s41598-018-33760-w.

587 [16] M.R. Ahmadian-Yazdi, M. Eslamian, Fabrication of semiconducting methylammonium Lead Halide
588 perovskite particles by spray technology, Nanoscale Res. Lett. 13 (2018) 4–11. doi:10.1186/s11671-
589 017-2430-0.

590 [17] Z. Wei, H. Chen, K. Yan, S. Yang, Inkjet printing and instant chemical transformation of a
591 $CH_3NH_3PbI_3$/nanocarbon electrode and interface for planar perovskite solar cells, Angew. Chem. Int.
592 53 (2014) 13239-13243. doi.org/10.1002/anie.201408638.

593 [18] E. Parvazian, A. Abdollah-zadeh, H. Reza, N. Taghavinia, Fabrication of perovskite solar cells based
594 on vacuum-assisted linear meniscus printing of $MAPbI_3$, Sol. Energy Mater. Sol. Cells. 191 (2019)
595 148–156. doi:10.1016/j.solmat.2018.11.012.

596 [19] Y. Liang, Y. Yao, X. Zhang, W. Hsu, Y. Gong, J. Shin, D. Eric, M. Dagenais, I. Takeuchi, Y. Liang,
597 Y. Yao, X. Zhang, W. Hsu, Fabrication of organic-inorganic perovskite thin films for planar solar
598 cells via pulsed laser deposition, AIP Adv. 6 (2016) 015001. doi.org/10.1063/1.4939621.

599 [20] H.G. Kim, H.B.R. Lee, Atomic layer deposition on 2D materials, Chem. Mater. 29 (2017) 3809-3826.
600 doi.org/10.1021/acs.chemmater.6b05103.

601 [21] M. He, B. Li, X. Cui, B. Jiang, Y. He, Y. Chen, D.O. Neil, P. Szymanski, M.A. Ei-sayed, J. Huang, Z.
602 Lin, Meniscus-assisted solution printing of large-grained perovskite films for high-efficiency solar
603 cells, Nat. Commun. 8 (2017) 1-10. doi.org/10.1038/ncomms16045.

604 [22] H. Liao, P. Guo, C. Hsu, M. Lin, B. Wang, L. Zeng, W. Huang, C. Myae, M. Soe, W. Su, M.J.

605 Bedzyk, M.R. Wasielewski, A. Facchetti, R.P.H. Chang, M.G. Kanatzidis, T.J. Marks, Enhanced
606 efficiency of hot-cast large-area planar perovskite solar cells/modules having controlled chloride
607 incorporation, Adv. Energy Mater. 7 (2017) 1601660. doi.org/10.1002/aenm.201601660.

608 [23] J. Ávila, C. Momblona, P.P. Boix, M. Sessolo, H.J. Bolink, Vapor-deposited perovskites: the route to
609 high-performance solar cell production, Joule 1 (2017) 431-442. doi.org/10.1016/j.joule.2017.07.014.

610 [24] J. Schlipf, L. Bießmann, L. Oesinghaus, E. Berger, E. Metwalli, J.A. Lercher, L. Porcar, P. Mu, In situ
611 monitoring the uptake of moisture into hybrid perovskite thin films, J. Phys. Chem. Lett. 9 (2018)
612 2015-2021. doi.org/10.1021/acs.jpclett.8b00687.

613 [25] T. Dewinggih, L. Muliani, R. Hidayat, The temperature effect on the working characteristics of solar
614 cells based on organometal halide perovskite crystals, J. Phys. Conf. Ser. 877 (2017) 012043.
615 doi.org/10.1088/1742-6596/877/1/012043.

616 [26] S. Lee, S. Kim, S. Bae, K. Cho, T. Chung, L.E. Mundt, S. Lee, S. Park, H. Park, M.C. Schubert, S.W.
617 Glunz, Y. Ko, Y. Jun, Y. Kang, H. Lee, D. Kim, UV degradation and recovery of perovskite solar
618 cells, Sci. Rep. 6 (2016) 38150. doi.org/10.1038/srep38150.

619 [27] Y. Zhou, Y. Zhao, Chemical stability and instability of inorganic halide perovskites, Energy Environ.
620 Sci. 12 (2019) 1495-1511. doi 10.1039/C8EE03559H.

621 [28] Q. Wang, N. Phung, D. Di Girolamo, P. Vivo, A. Abate, Enhancement in lifespan of halide perovskite
622 solar cells, Energy Environ. Sci. 12 (2018) 865-886. doi: 10.1039/C8EE02852D.

623 [29] X. Zheng, Y. Bai, S. Xiao, X. Meng, Strategies for improving efficiency and stability of perovskite
624 solar cells, MRS Adv. 2 (2017) 3051-3060. doi.org/10.1557/adv.2017.485.

625 [30] P. Zhang, F. Yang, G. Kapil, C.H. Ng, T. Ma, S. Hayase, Preparation of perovskite films under liquid
626 nitrogen atmosphere for high efficiency perovskite solar cells, ACS Sustain. Chem. Eng. 7 (2019)
627 3956-3961. doi.org/10.1021/acssuschemeng.8b05139.

628 [31] Q. Ma, S. Huang, S. Chen, M. Zhang, C.F.J. Lau, M.N. Lockrey, H.K. Mulmudi, Y. Shan, J. Yao, J.
629 Zheng, X. Deng, K. Catchpole, M.A. Green, A.W.Y. Ho-Baillie, The effect of stoichiometry on the
630 stability of inorganic cesium lead mixed-halide perovskites solar cells, J. Phys. Chem. C. 121 (2017)
631 19642-19649.

632 [32] R. Yang, L. Zhang, Y. Cao, Y. Miao, Y. Ke, Y. Wei, Q. Guo, Inhomogeneous degradation in metal
633 halide perovskites, Appl. Phys. Lett. 111 (2017) 073302. doi.org/10.1063/1.4999630.

634 [34] C. Momblona, O. Malinkiewicz, C. Roldán-Carmona, A. Soriano, L. Gil-Escrig, E. Bandiello, M.
635 Scheepers, E. Edri, H.J. Bolink, Efficient methylammonium lead iodide perovskite solar cells with
636 active layers from 300 to 900 nm, APL Mater. 2 (2014) 081504. doi.org/10.1063/1.4890056.

637 [35] C. Chen, H. Kang, S. Hsiao, P. Yang, K. Chiang, H. Lin, Efficient and uniform planar-type perovskite
638 solar cells by simple sequential vacuum deposition, Adv. Mater. 26 (2014) 6647-6652.
639 doi.org/10.1002/adma.201402461.

640 [36] J. Borchert, I. Levchuk, L.C. Snoek, M.U. Rothmann, H.J. Snaith, C.J. Brabec, L.M. Herz, M.B.
641 Johnston, impurity tracking enables enhanced control and reproducibility of hybrid perovskite vapor
642 deposition, ACS Appl. Mater. Interfaces 11 (2019) 28851-28857. doi.org/10.1021/acsami.9b07619.

643 [37] K. Yonezawa, K. Yamamoto, T.S. Ripolles, M. Karakawa, T. Kuwabara, K. Takahashi, S. Hayase, T.
644 Taima, Improved reproducibility and intercalation control of efficient planar inorganic perovskite
645 solar cells by simple alternate vacuum deposition of PbI_2 and CsI, Acs Omega 2 (2017) 4464-4469.

doi:10.1021/acsomega.7b00814.

[38] M. Á. Reinoso, C. A. Otálora, G. Gordillo, Improvement properties of hybrid halide perovskite thin films prepared by sequential evaporation for planar solar cells, Mater. 12 (2019) 1394. doi.org/10.3390/ma12091394.

[39] J.B. Patel, R.L. Milot, A.D. Wright, L.M. Herz, M.B. Johnston, Formation dynamics of $CH_3NH_3PbI_3$ perovskite following two-step layer deposition, J. Phys. Chem. Lett. 7 (2016) 96-102. doi.org/10.1021/acs.jpclett.5b02495.

[40] J.N. Fru, N. Nombona, M. Diale, Synthesis and characterisation of methylammonium lead tri-bromide perovskites thin films by sequential physical vapor deposition, Phys. B Phys. Condens. Matter. 578 (2020) 411884. doi.org/10.1016/j.physb.2019.411884.

[41] D. Shi, V. Adinolfi, R. Comin, M. Yuan, E. Alarousu, A. Buin, Y. Chen, S. Hoogland, A. Rothenberger, K. Katsiev, Y. Losovyj, X. Zhang, P.A. Dowben, O.F. Mohammed, E.H. Sargent, O.M. Bakr, Low trap-state density and long carrier diffusion in organolead trihalide perovskite single crystals, Sci. 347 (2015) 519-522. doi 10.1126/science.aaa2725.

[42] M.I. Saidaminov, A.L. Abdelhady, B. Murali, E. Alarousu, V.M. Burlakov, W. Peng, I. Dursun, L. Wang, Y. He, G. MacUlan, A. Goriely, T. Wu, O.F. Mohammed, O.M. Bakr, High-quality bulk hybrid perovskite single crystals within minutes by inverse temperature crystallization, Nat. Commun. 6 (2015) 1-6. doi.org/10.1038/ncomms8586.

[43] N.J. Jeon, J.H. Noh, Y.C. Kim, W.S. Yang, S. Ryu, S. Il Seok, Solvent engineering for high-performance inorganic–organic hybrid perovskite solar cells, Nat. Mater. 13 (2014) 897-903. doi.org/10.1038/nmat4014.

[44] K. Frohna, T. Deshpande, J. Harter, W. Peng, B.A. Barker, J.B. Neaton, S.G. Louie, O.M. Bakr, D. Hsieh, M. Bernardi, Inversion symmetry and bulk Rashba effect in methylammonium lead iodide perovskite single crystals, Nat. Commun. 9 (2018) 1-9. doi.org/10.1038/s41467-018-04212-w.

[45] G.K. Williamson, W.H. Hall, X-ray line broadening from filed aluminium and wolfram, Acta Metall. 1 (1953) 22-31. doi.org/10.1016/0001-6160(53)90006-6.

[46] T.W. Jones, A. Osherov, M. Alsari, M. Sponseller, B.C. Duck, Y.K. Jung, C. Settens, F. Niroui, R. Brenes, C. V. Stan, Y. Li, M. Abdi-Jalebi, N. Tamura, J.E. MacDonald, M. Burghammer, R.H. Friend, V. Bulović, A. Walsh, G.J. Wilson, S. Lilliu, S.D. Stranks, Lattice strain causes non-radiative losses in halide perovskites, Energy Environ. Sci. 12 (2019) 596-606. doi 10.1039/C8EE02751J.

[47] G.K. Williamson, R.E. Smallman, III. Dislocation densities in some annealed and cold-worked metals from measurements on the X-ray debye-scherrer spectrum, Philos. Mag. 1 (1956) 34-46. doi 10.1080/14786435608238074.

[48] F. Haque, M. Wright, A. Mahmud, H. Yi, D. Wang, L. Duan, C. Xu, A. Uddin, Effects of hydroiodic acid concentration on the properties of $CsPbI_3$ perovskite solar cells, ACS Omega 3 (2018) 11937-11944. doi.org/10.1021/acsomega.8b01589.

[49] C. Ran, J. Xu, W. Gao, C. Huang, S. Dou, Defects in metal triiodide perovskite materials towards high-performance solar cells: origin, impact, characterization, and engineering, Chem. Soc. Rev. 47 (2018) 4581-4610. doi 10.1039/C7CS00868F.

[50] P. Fan, D. Gu, G. Liang, J. Luo, J. Chen, Z. Zheng, High-performance perovskite $CH_3NH_3PbI_3$ thin films for solar cells prepared by single-source physical vapour deposition, Sci. Rep. 6 (2016) 29910. doi.org/10.1038/srep29910.

[51] Q. Chen, H. Zhou, T. Bin Song, S. Luo, Z. Hong, H.S. Duan, L. Dou, Y. Liu, Y. Yang, Controllable self-induced passivation of hybrid lead iodide perovskites toward high performance solar cells, Nano lett. 14 (2014) 4158-4163. doi.org/10.1021/nl501838y.

[52] B. Park, N. Kedem, M. Kulbak, D.Y. Lee, W.S. Yang, N.J. Jeon, J. Seo, G. Kim, K.J. Kim, T.J. Shin, G. Hodes, D. Cahen, S. Il Seok, Understanding how excess lead iodide precursor improves halide perovskite solar cell performance, Nat. Commun. 9 (2018) 1-8. doi.org/10.1038/s41467-018-05583-w.

[53] T.J. Jacobsson, J.P. Correa-Baena, E. Halvani Anaraki, B. Philippe, S.D. Stranks, M.E.F. Bouduban, W. Tress, K. Schenk, J. Teuscher, J.E. Moser, H. Rensmo, A. Hagfeldt, Unreacted PbI_2 as a double-edged sword for enhancing the performance of perovskite solar cells, J. Am. Chem. Soc. 138 (2016) 10331-10343. doi.org/10.1021/jacs.6b06320.

[54] U. Kwon, M.M. Hasan, W. Yin, D. Kim, U. Thakur, N.Y. Ha, S. Lee, T.K. Ahn, H.J. Park, Investigation into the advantages of pure perovskite film without PbI_2 for high performance solar cell, Sci. Rep. 6 (2016) 35994. doi.org/10.1038/srep35994.

[55] T.J. Jacobsson, L.J. Schwan, M. Ottosson, A. Hagfeldt, T. Edvinsson, Determination of thermal expansion coefficients and locating the temperature-induced phase transition in methylammonium lead perovskites using X-ray diffraction, Inorg. Chem. 54 (2015) 10678–10685. doi.org/10.1021/acs.inorgchem.5b01481.

[56] B. Dunn, Y. Yang, M. Wang, L. Zuo, H. Guo, N. De Marco, D.S. Ginger, S. Dong, S. Jariwala, D.W. deQuilettes, R. DeBlock, Polymer-modified halide perovskite films for efficient and stable planar heterojunction solar cells, Sci. Adv. 3 (2017) e1700106. doi:10.1126/sciadv.1700106.

[57] K.H. Hendriks, J.J. Van Franeker, B.J. Bruijnaers, J.A. Anta, M.M. Wienk, R.A.J. Janssen, 2-Methoxyethanol as a new solvent for processing methylammonium lead halide perovskite solar cells, J. Mater. Chem. A. 5 (2017) 2346–2354. doi:10.1039/C6TA09125C.

[58] W. Zhao, D. Yang, Z. Yang, S. (Frank) Liu, Zn-doping for reduced hysteresis and improved performance of methylammonium lead iodide perovskite hybrid solar cells, Mater. Today Energy. 5 (2017) 205–213. doi:10.1016/j.mtener.2017.06.009.

[59] N. Liu, Q. Du, G. Yin, P. Liu, L. Li, H. Xie, C. Zhu, Y. Li, H. Zhou, W. Bin Zhang, Q. Chen, Extremely low trap-state energy level perovskite solar cells passivated using NH 2 -POSS with improved efficiency and stability, J. Mater. Chem. A. 6 (2018) 6806–6814. doi:10.1039/c7ta11345e.

[60] K. Meerholz, S. Van Smaalen, F. Panzer, Impact of excess PbI_2 on the structure and the temperature dependent optical properties of methylammonium lead iodide perovskites, J. Mater. Chem. C. 6 (2018) 7512-7519. doi 10.1039/C8TC02237B.

[61] H. Zhang, M. Tao, B. Gao, W. Chen, Q. Li, Q. Xu, S. Dong, Preparation of $CH_3NH_3PbI_3$ thin films with tens of micrometer scale at high temperature, Sci. Rep. 7 (2017) 1-9. doi.org/10.1038/s41598-017-09109-0.

[62] M. Oztas, Influence of grain size on electrical and optical properties of InP films, Chin. Phys. Lett. 25 (2008) 4090. doi.org/10.1088/0256-307X/25/11/069.

[63] V. D'Innocenzo, A.R. Srimath Kandada, M. De Bastiani, M. Gandini, A. Petrozza, Tuning the light emission properties by band gap engineering in hybrid lead halide perovskite, J. Am. Chem. Soc. 136 (2014) 17730-17733. doi.org/10.1021/ja511198f.

[64] W. Shockley, H.J. Queisser, Detailed balance limit of efficiency of p-n junction solar cells, J. Appl.

730 Phys. 32 (1961) 510. doi: 10.1063/1.1736034

731 [65] W.E. Sha, X. Ren, L. Chen, W.C. Choy, The efficiency limit of $CH_3NH_3PbI_3$ perovskite solar cells.
732 Appl. Phys. Lett. 106 (2015) 221104. doi.org/10.1063/1.4922150.

733 [66] L. Kong, G. Liu, J. Gong, Q. Hu, R.D. Schaller, P. Dera, D. Zhang, Z. Liu, W. Yang, K. Zhu, Y.
734 Tang, C. Wang, S.-H. Wei, T. Xu, H. Mao, Simultaneous band-gap narrowing and carrier-lifetime
735 prolongation of organic–inorganic trihalide perovskites, Proc. Natl. Acad. Sci. 113 (2016) 8910-
736 8915. doi.org/10.1073/pnas.1609030113.

737 [67] E.A. Davis, N.F. Mott, Conduction in non-crystalline systems V. Conductivity, optical absorption and
738 photoconductivity in amorphous semiconductors, Philos. Mag. 22 (1970) 903–922.
739 doi:10.1080/14786437008221061.

740 [68] R. Robles, C. Katan, D. Sapori, L. Pedesseau, J. Even, S. Chimiques, C. Université, D.R. Rennes,
741 I.C.N. Institut, C. De Nanociencia, Rashba and Dresselhaus effects in hybrid organic–inorganic
742 perovskites: from basics to devices, ACS Nano. 9 (2015) 11557-11567.
743 doi.org/10.1021/acsnano.5b04409.

744 [69] T. Etienne, E. Mosconi, F. De Angelis, Dynamical origin of the Rashba effect in organohalide lead
745 perovskites: a key to suppressed carrier recombination in perovskite solar cells, J. Phys. Chem. Lett. 7
746 (2016) 1638-1645. doi.org/10.1021/acs.jpclett.6b00564.

747 [70] F. Zheng, L.Z. Tan, S. Liu, A.M. Rappe, Rashba spin–orbit coupling enhanced carrier lifetime in
748 $CH_3NH_3PbI_3$, Nano lett. 15 (2015) 7794-7800. doi.org/10.1021/acs.nanolett.5b01854.

749 [71] C. V. Ramana, R.J. Smith, O.M. Hussain, Grain size effects on the optical characteristics of pulsed-
750 laser deposited vanadium oxide thin films, Phys. Status Solidi Appl. Res. 199 (2003) 5–7.
751 doi:10.1002/pssa.200309009.

752 [72] S.M. Jain, B. Philippe, E.M.J. Johansson, B.W. Park, H. Rensmo, T. Edvinsson, G. Boschloo, Vapor
753 phase conversion of PbI_2 to $CH_3NH_3PbI_3$: Spectroscopic evidence for formation of an intermediate
754 phase, J. Mater. Chem. A. 4 (2016) 2630–2642. doi:10.1039/c5ta08745g.

755 [73] G. Abdelmageed, L. Jewell, K. Hellier, L. Seymour, B. Luo, F. Bridges, J.Z. Zhang, S. Carter,
756 Mechanisms for light induced degradation in $MAPbI_3$ perovskite thin films and solar cells, Appl.
757 Phys. Lett. 109 (2016) 0–5. doi:10.1063/1.4967840.

758 [74] M.A. Lampert, Simplified theory of space-charge-limited currents in an insulator with traps, Phys.
759 Rev. 103 (1956) 1648–1656. doi:10.1103/PhysRev.103.1648.

760 [75] L. Zhou, W. Lanford, A.T. Ping, I. Adesida, J.W. Yang, A. Khan, Low resistance Ti/Pt/Au ohmic
761 contacts to p-type GaN, Appl. Phys. Lett. 76 (2000) 3451–3453. doi:10.1063/1.126674.

762 [76] S. Gupta, P. Paramahans Manik, R. Kesh Mishra, A. Nainani, M.C. Abraham, S. Lodha, Contact
763 resistivity reduction through interfacial layer doping in metal-interfacial layer-semiconductor
764 contacts, J. Appl. Phys. 113 (2013). doi:10.1063/1.4811340.

765 [77] M.I. Saidaminov, A.L. Abdelhady, B. Murali, E. Alarousu, V.M. Burlakov, W. Peng, I. Dursun, L.
766 Wang, Y. He, G. Maculan, A. Goriely, T. Wu, O.F. Mohammed, O.M. Bakr, High-quality bulk hybrid
767 perovskite single crystals within minutes by inverse temperature crystallization, Nat. Commun. 6
768 (2015) 1-6. doi.org/10.1038/ncomms8586.

769

Highlights

- Simplified growth of $MAPbI_3$ by sequential physical vapor deposition of PbI_2 and MAI single layers.
- Prolong annealing of $MAPbI_3$ causes reversible phase transformation between $MAPbI_3$ and PbI_2.
- Optimization of the stoichiometry of $MAPbI_3$ by precise thickness regulation.
- Trap density and carrier mobility of $MAPbI_3$ thin films by space charge limited current theory.

All authors declare no conflict of interest.